The Astrophysical Journal Letters, 908:L2 (12pp),2021 February 10 https://doi.org/10.3847/2041-8213/abd53f

Identifying Black Hole Central Engines in Gamma-Ray Bursts

Vidushi Sharma, Shabnam Iyyani, and Dipankar Bhattacharya
Inter-University Center for Astronomy and Astrophysics, Pune, Maharashtra 411007, India; vidushi@iucaa.in, shabnam@iucaa.in
Received 2020 August 17; revised 2020 December 12; accepted 2020 December 20; published 2021 February 5

Abstract

The nature of the gamma-ray burst (GRB) central engine still remains an enigma. Entities widely believed to be capable of powering the extreme jets are magnetars and black holes. The maximum rotational energy that is available in a millisecond magnetar to form a jet is $\sim 10^{52}$ erg. We identify eight long GRBs whose jet-opening angle-corrected energetics of the prompt emission episode are $>10^{52}$ erg with high confidence level and, therefore, their central engines are expected to be black holes. The majority of these GRBs present significant emission in the sub-GeV energy range. The X-ray afterglow light curves of these bursts do not show any shallow decay behavior such as a plateau; however, a few cases exhibit flares and multiple breaks instead of a single power-law decay. For a minimum mass of the black hole ($\sim 2\,M_\odot$), we find the efficiency of producing a jet from its rotational energy to range between 2% and 270%. Highly energetic jets requiring high efficiencies implies that either the mass of these black holes are much larger or there are, in addition, other sources of energy that power the jet. By considering the Blandford–Znajek mechanism of jet formation, we estimate the masses of these black holes to range between ~2 and 60 $M_\odot$. Some of the lighter black holes formed in these catastrophic events are likely candidates to lie in the mass-gap region (2–5 $M_\odot$).

Unified Astronomy Thesaurus concepts: Gamma-ray bursts (629); Black holes (162); Magnetars (992); High energy astrophysics (739)

1. Introduction

Gamma-ray bursts (GRBs) are extremely luminous sources with isotropic equivalent energies ranging between 10^{47} and 10^{55} erg (Ajello et al. 2019). These observations suggest that the central engine of these bursts should be capable of launching highly energetic jets that significantly exceed the Eddington luminosity. The smallest time variability observed in GRB light curves is of a few milliseconds, which suggests emission originating from compact sources of radius of the order of $\sim 10^8$–10^9 cm (MacLachlan et al. 2013). Broadly, two types of central engines are considered for GRBs: (i) a hyper-accreting stellar-mass black hole (Woosley 1993; Narayan et al. 2001; McKinney 2005), and (ii) a rapidly spinning, highly magnetized, neutron star (NS) or "fast magnetar" (Duncan & Thompson 1992; Usov 1992; Metzger et al. 2011).

Generally, inferences regarding the plausible central engine of GRBs are made by studying the various features such as plateau, flares, and steep decays observed in the X-ray afterglow flux light curves detected by Neil Gehrels Swift Observatory's X-Ray Telescope (XRT; Rowlinson et al. 2014; Nathanail et al. 2016; Lei et al. 2017; Li et al. 2018; Sarin et al. 2019; Zhao et al. 2020). However, such a piecemeal study of the afterglow light curves leaves several unanswered questions regarding the mechanism of powering the relativistic jets. Both the magnetar and black hole central engine models can explain most of the features present in the XRT light curves, which results in ambiguity and uncertainty regarding the central engine of the GRB. On the other hand, a robust method is to compare the energetics of the GRB with both the central engine models (Cenko et al. 2011).

Magnetars are NSs with high magnetic fields (10^{15} G) (Duncan & Thompson 1992; Usov 1992; Metzger et al. 2011). To power a GRB, a magnetar must also be spinning rapidly. The spin frequency distribution of accreting millisecond X-ray pulsars are found to show a sharp cutoff at 730 Hz, which corresponds to a periodicity, $P_{ns} \sim 1$ ms (Hessels et al. 2006; Chakrabarty 2008; Papitto et al. 2014; Patruno et al. 2017). The mean of the mass distribution of millisecond pulsars is found to be $M_{ns} = 1.48 \pm 0.2\,M_\odot$ (Özel et al. 2012). The equation of state of an NS gives a corresponding maximum possible radius (R_{ns}) of the NS to be ~12 km. The rotational energy of the magnetar that powers the GRB jet, normalized to typical observed parameters, is estimated as to be

$$E_{\rm rot} = \frac{1}{2} I \Omega^2 \approx 3 \times 10^{52}\ {\rm erg} \left(\frac{M_{\rm ns}}{1.5 M_\odot}\right) \left(\frac{R_{\rm ns}}{12\ {\rm km}}\right)^2 \left(\frac{P_{\rm ns}}{1\ {\rm ms}}\right)^{-2} \quad (1)$$

where I is the moment of inertia of the NS calculated as $\frac{2}{5} M_{\rm ns} R_{\rm ns}^2$, and Ω is the rotational speed. More massive NSs with $M_{ns} = 2\,M_\odot$ can have P_{ns} as small as 0.7 ms, and E_{rot} may reach $\sim 10^{53}$ erg. Such a short period is not yet observed in any millisecond pulsar. Also, the maximum rotational energy from the magnetar decreases rapidly when the magnetar mass is above the maximum stable mass limit of ~2.1–2.4 $M_\odot$ (supramassive NSs; see Figure 8 in Metzger 2017). In addition, Metzger et al. (2018; see also Beniamini et al. 2017) has shown that when considering scenarios like the fall-back accretion on to a magnetar, the process of accretion does not significantly alter the maximum rotational energy that is available from a magnetar in comparison to an isolated (non-accreting) magnetar, that is spinning near the breakup value of 1 ms. Thus, theoretically, moderately higher values of E_{rot} can be expected from the magnetar; however, while considering realistic scenarios like fall-back accretion and based on the observation of the various parameters like mass and periodicity of the NSs, we find the E_{rot} to be roughly around a few times 10^{52} erg (consistent with Equation (1)).

The rotational energy of the magnetar, apart from powering the GRB jet, is also lost through magnetospheric winds and gravitational waves. Thus, by considering equipartition,[1] we find it very reasonable to consider that the maximum extractable rotational energy of magnetar that can be channelized into powering a relativistic jet is $E_{rot,jet} = 1 \times 10^{52}$ erg. Therefore, any GRB with a total burst energy exceeding this energy budget can be considered to not possess a magnetar but instead a black hole as its central engine.

In this Letter, we use the burst energetics of the prompt gamma-ray emission of the GRBs to identify the bursts with black holes as their central engines. The bursts' energy calculations in this Letter use the standard ΛCDM cosmology, with cosmological parameters $H_0 = 67.4 \pm 0.5$ km s^{-1} Mpc^{-1}, $\Omega_{vac} = 0.685$ and $\Omega_m = 0.315$ (Aghanim et al. 2020).

2. Sample Selection

GRBs with known redshifts detected by the Fermi gamma-ray space telescope[2] are presented in the online GRB table of Jochen Greiner.[3] Fermi observations provide a spectral coverage spanning over several decades of energy between a few keV to several GeV. This allows us to model the spectrum of the prompt emission better and estimate the bolometric energy flux of the burst. Our sample consists of 135 GRBs with redshift information detected by Fermi during the years 2008–2019. The various steps undertaken to identify the GRBs with black hole central engines are described in the section below and are also summarized in the flowchart presented in Figure 1.

3. Methodology of Identification

3.1. Isotropic Prompt Gamma-Ray Emission $E_{\gamma,iso}$

Assuming an isotropic emission, the total gamma-ray energy released during the prompt phase of the burst is termed as $E_{\gamma,iso}$. The isotropic equivalent energy is found as (Bloom et al. 2001)

$$E_{g,\mathrm{iso}} = \left(\frac{4\pi D_L^2}{1+z}\right) F_{\mathrm{bol}} \quad (2)$$

where, F_{bol} is the bolometric fluence, and D_L is the luminosity distance of the burst at a redshift z.

In total, there are 104 Gamma-ray Burst Monitor (GBM)-only detected and 31 Large Area Telescope (LAT)+GBM-detected GRBs with known redshifts. For this work, we conducted the time-integrated spectral analyses of all the 31 LAT-detected GRBs and six GBM-only detected GRBs whose spectral parameters are not updated in the Fermi catalog. The spectral analyses of the GBM-only cases are done using the Band model, whereas the joint time-integrated spectral analyses using the GBM and LAT data are performed using various models such as Band, Band + Power-law, and Band + Cutoff-powerlaw. The best-fit model is then used for the fluence estimation. In Fermi/GBM catalog, the fluence is reported for 10–1000 keV energy range, which gives an underestimation of the total energy released during the burst. Therefore, the bolometric fluences of all the bursts are estimated within the energy limits of 1 keV and 1 GeV.[4] Note that for 98 GBM-only detected GRBs, the bolometric fluences are estimated using the spectral parameters for the Band function fits and the T_{90} given in the Fermi catalog.

The isotropic equivalent burst energies of the 135 GRBs thus obtained are then compared with the maximum possible rotational energy limit of a magnetar (3×10^{52} erg) and a total of 105 hyper-energetic GRBs are found to exceed this energy budget (Figure 2(a)). We note that no short GRB made into this list of hyper-energetic GRBs.

3.2. Beam-corrected Prompt Emission $E_{\gamma,beam}$

GRB outflows are collimated relativistic jets, which means that the exact burst energy is the amount of energy that is ejected into the solid angle forming the jet. This is referred to as the beam-corrected prompt emission, $E_{\gamma,beam}$. This is estimated by multiplying the isotropic burst energy, $E_{\gamma,iso}$, with the beaming correction factor (Frail et al. 2001) given as

$$f_b = 1 - \cos\theta_j \quad (3)$$

where θ_j is the opening angle of the jet. In this work, we consider only the uniform (top-hat) jet scenario, which is the typical model considered in literature (see Appendix B for a discussion about structured jets).

The jet-opening angle values for bursts that are already reported in the literature until 2020 June are used as it is (51 cases[5]) and in the remaining cases, the jet-opening angle is estimated by using the time of jet breaks observed in Neil Gehrels Swift Observatory/XRT afterglow observations (26 cases). In cases where the jet break is not observed (27 cases), the last data point in the XRT observation is used to estimate the lower limit of the possible jet-opening angle of that GRB (Sari et al. 1999; Frail et al. 2001). In Appendix B, we have discussed the different caveats that are involved in the $E_{\gamma,beam}$ estimation.

3.2.1. Jet-opening Angle Calculation

The online XRT repository[6] is used for extracting the energy flux light curves in 0.3–10 keV energy range and the time of the jet break. The XRT products are created using automatic analysis described in Evans et al. (2007, 2009). Using the above information, the jet-opening angle is estimated under the assumption of standard afterglow model, on-axis viewing geometry, and a uniform jet, by the following expression

[1] In a more realistic scenario, only a small fraction of the rotational energy is expected to be converted into the jet (Meszaros 2006) and therefore, the burst energy limit of 10^{52} erg presents an elevated upper limit for the jet produced by a magnetar.

[2] https://heasarc.gsfc.nasa.gov/W3Browse/fermi/fermigbrst.html

[3] http://www.mpe.mpg.de/~jcg/grbgen.html

[4] In LAT-detected cases, wherever the highest energetic photon detected exceeded 1 GeV, the fluence was estimated in the energy range extending up until that highest observed energy value.

[5] We have used the beaming angles reported in the literature, which were estimated by modeling the optical, radio, or late-time X-ray afterglow observations by considering a uniform jet with on-axis and off-axis (particularly, Zhang et al. 2015) viewing geometry. In the case of GRBs, where multiple values of θ_j are reported, we have used either the well-constrained value or the lower estimate, as that would provide a more stringent constraint on the energy.

[6] https://www.swift.ac.uk/xrt_curves/

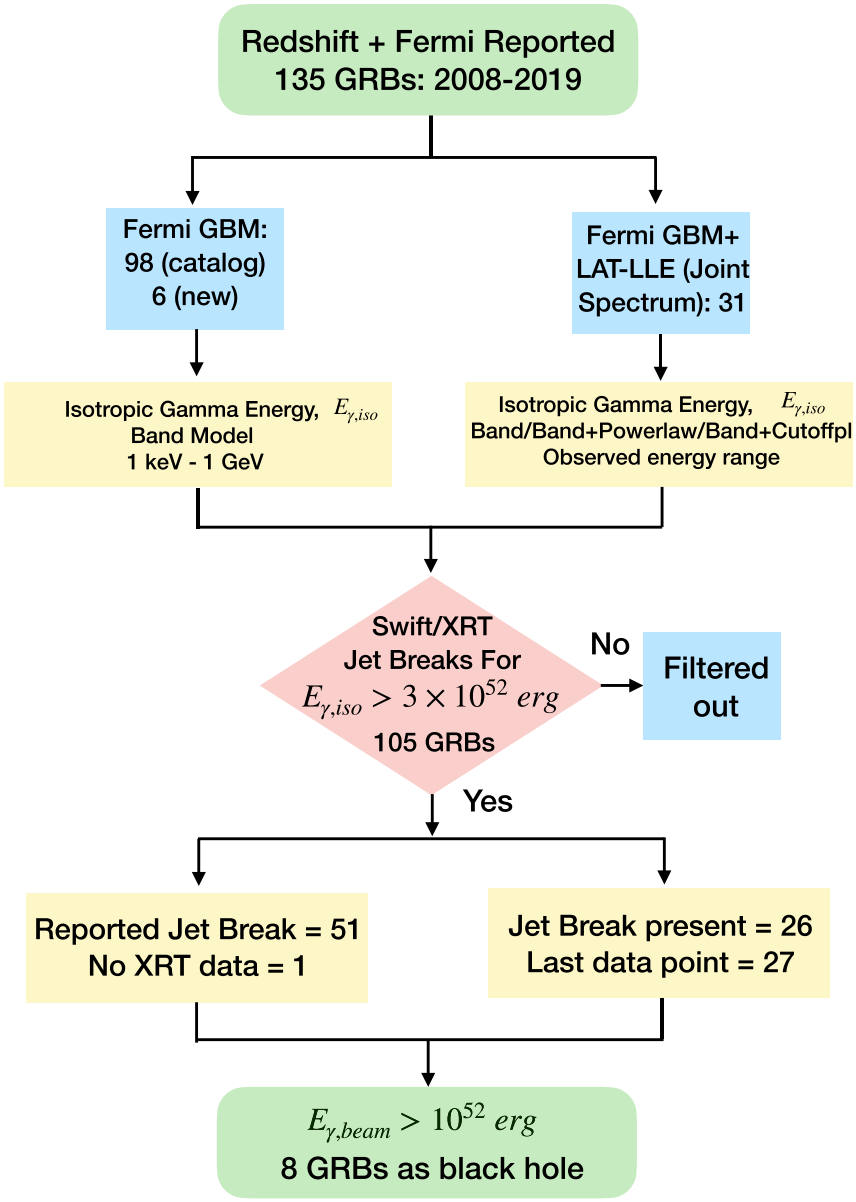

Figure 1. Flowchart of sample selection process.

(Sari et al. 1999; Wang et al. 2015)

$$q \approx 0.057 \left(\frac{t_j}{1\ \mathrm{day}}\right)^{3/8} \left(\frac{1+z}{2}\right)^{-3/8} \left(\frac{E_{g,\mathrm{iso}}}{10^{53}\ \mathrm{erg}}\right)^{-1/8} \left(\frac{\eta}{0.2}\right)^{1/8} \left(\frac{n_p}{0.1\ \mathrm{cm}^{-3}}\right)^{1/8} \quad (4)$$

where t_j is the time of jet break in days, η is a measure of how efficiently the total energy of the burst is converted into radiation, and n_p is ambient medium density. The estimate of θ_j is weakly dependent on η and n_p which are largely unknown. Following the methodology in Goldstein et al. (2016), we assume a broad uniform distribution for η from 5% to 95%, considering the earlier reported range of radiation efficiencies (Cenko et al. 2011; Racusin et al. 2011). Based on the limited number of estimates made for n_p previously, a log-normal distribution with mean $\log_{10}(0.1)$ and standard deviation 1 is assumed. In this work, we have also considered a uniform distribution for t_j within its uncertainty limits obtained from the observations. Thus, the probability distribution of θ_j is built by evaluating θ_j (Equation (4)) for each Monte Carlo sampled set of values of t_j, η and n_p from their respective probability distributions. By fitting a Gaussian distribution function to the obtained distribution, we obtain the mean value of θ_j and the standard deviation as its uncertainty. The distribution of θ_j obtained for the GRBs where the jet break is observed or reported earlier is shown in Figure 2(b).

In case of GRBs, where the jet break is not observed in XRT energy flux light curve, using the time of the last data point in the light curve we estimate the distribution of lower limit of θ_j for the GRB using the abovementioned assumptions and Monte Carlo method. The value obtained after subtracting the standard deviation from the mean of the distribution is considered as $q_{,\mathrm{min}}$ for the GRB.

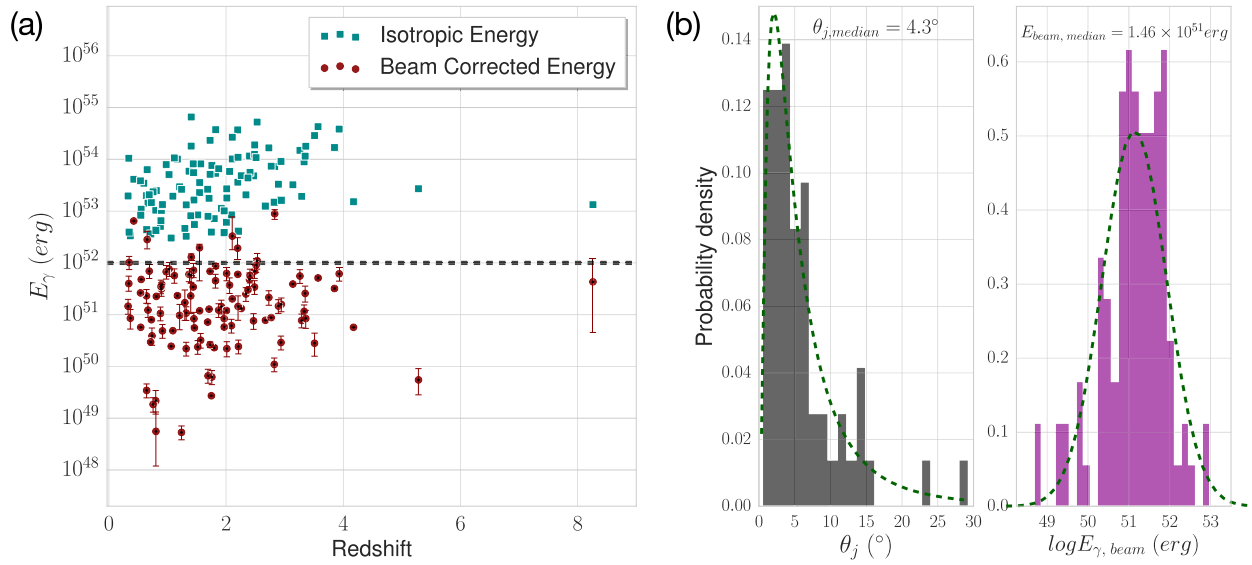

Figure 2. (a) The E_{iso} and $E_{\gamma,beam}$ of the prompt emission of the 105 hyper-energetic GRBs are shown in green squares and red circles, respectively. The horizontal gray dashed line marks 10^{52} erg. (b) The distributions of θ_j and $E_{\gamma,beam}$ of the 105 hyper-energetic GRBs are shown in the left and right panels of the plot, respectively. The log-normal fits to the respective distributions are shown in dashed green lines. The means of θ_j and $E_{\gamma,beam}$ distributions are 2°. 1 ± 0°. 9 and $(1.9 \pm 4.2) \times 10^{51}$ erg, respectively.

Table 1
Properties of Hyper-energetic GRBs

GRB Name	T_{90} (Fermi) (s)	z	Fluence 10^{-4} erg cm^{-2}	$E_{\gamma,iso}$ 10^{52} erg	θ_j[a] (°)	δ[a]	$E_{\gamma,beam}$ 10^{52} erg	Confidence[b] Level	$M_*/M_\odot$	Swift/ XRT Feature
190114C	116.354	0.425	$8.5^{+0.3}_{0.3}$	$41.2^{+1.4}_{1.3}$	> 32.5	0.18	$> 6.5^{+0.2}_{0.2}$	> 99.99%	40–60	3 Breaks
180720B	48.897	0.654	$5.4^{+0.5}_{0.4}$	$63.3^{+5.7}_{5.2}$	$> 17.2^{+2.6}_{2.6}$	L	$> 2.8^{+1.2}_{0.9}$	99.6%	5–7	Flare,3 Breaks
170214A[c]	122.882	2.53	$3.5^{+0.2}_{0.1}$	$525.7^{+23.0}_{21.0}$	$> 3.7^{+0.6}_{0.6}$	L	$> 1.1^{+0.4}_{0.3}$	61.5%	2.14−3	Straight line
160625B[c,d]	453.385	1.406	$12.4^{+0.4}_{0.4}$	$657.8^{+22.2}_{20.6}$	$3.6^{+0.2}_{0.2}$	0.98	$1.3^{+0.2}_{0.2}$	98.3%	2.14−2.22	1 Break
120624B	271.364	2.197	$3.1^{+0.6}_{0.5}$	$371.1^{+74.6}_{57.4}$	$> 5.8^{+0.9}_{0.9}$	L	$> 1.9^{+1.1}_{0.7}$	94.6%	3–5	A few points
110731A	7.485	2.83	$0.4^{+0.1}_{0.1}$	$72.9^{+14.5}_{13.2}$	$28.9^{+0.0}_{0.7}$	0.86	$8.9^{+1.8}_{2.0}$	99.9%	12–17	Flare,3 Breaks
090926A[d]	13.76	2.106	$2.4^{+0.03}_{0.03}$	$267.4^{+33.8}_{26.2}$	9^{+4}_{2}	0.98	$3.3^{+4.4}_{1.5}$	90.8%	4–6	Straight line
090102	26.624	1.547	$0.4^{+0.1}_{0.1}$	$22.8^{+1.6}_{1.7}$	$23.9^{+1.1}_{12.1}$	0.25	$2.0^{+0.3}_{1.5}$	85%	9–13	1 Break

Notes. All the errors reported above are 68% confidence intervals of the estimated parameters.
[a] The references are provided for the θ_j values, and the kinetic energy estimates that are used to evaluate the δ values that are adopted in this work. GRB 190114C—Misra et al. (2019); GRB 180720B—this work;GRB 170214A—this work;GRB 160625B—Alexander et al. (2017; see also Cunningham et al. 2020, where θ_j estimation ranges from 1.26 to 3.90 deg and can lower the beam-corrected total energy of the burst.); GRB 120624B—this work; GRB 110731A—Zhang et al. (20 GRB 090926A—Cenko et al. (2011), GRB 090102—Zhang et al. (2015).
[b] The confidence levels of the reported values/ lower limits of the $E_{\gamma,beam}$ to lie above the considered energy budget limit of 10^{52} erg are listed. The probability distribution of $E_{\gamma,beam}$ of each GRB is generated by randomly drawing the parameters from their respective Gaussian distributions of $E_{\gamma,iso}$ and θ_j with value and its error as mean and standard deviation for a million runs. The obtained probability distribution is used to estimate the confidence interval such that the probability of $E_{\gamma,beam} > 10^{52}$ erg.
[c] In these GRBs, the possible lower limit of black hole mass is considered to be 2.14 $M_\odot$. The estimated lower limits are less than the minimum possible mass of stellar mass black holes.
[d] GRB 090926A was the only hyper-energetic Fermi GRB that was identified in Cenko et al. (2011) to pose a severe challenge to the magnetar central engine mod

3.3. Result

The isotropic equivalent energies observed in prompt gamma-ray emission ($E_{\gamma,iso}$) for the 105 GRBs that exceed the magnetar energy budget (10^{52} erg) are shown in Figure 2(a). After beam correction, we observe a wide distribution of beam-corrected energies $E_{\gamma,beam}$ in the prompt phase (Figure 2(a)).The distribution of the $E_{\gamma,beam}$ of these GRBs is shown in Figure 2(b).

The total burst energy is the sum of $E_{\gamma,beam}$ and the remaining kinetic energy of the jet estimated from the afterglow emissions. By using just the prompt gamma-ray energetics, we find eight long GRBs whose $E_{\gamma,beam}$ exceed or are nearly equivalent to the limit of the maximum possible rotational energy of the magnetar that can be converted into a jet (1×10^{52} erg). Following Racusin et al. (2011) and Cenko et al. (2011), it is reasonable to consider that these bright, Fermi-detected GRBs possess high radiation efficiencies ($\delta > 0.2$), which in turn suggests that the total burst energies in these GRBs can be $E_{burst} \sim E_{\gamma,beam}$. This assures that the total burst energies of these GRBs are even greater than this limit ($>10^{52}$ erg) and thereby confirm that the central engine or the remnant of the core collapse of the massive progenitor star of these GRBs are black holes. These GRBs, along with their observational features, are listed in Table 1.

4. Discussion

Below, we discuss the various properties of the prompt, afterglow emissions, and the black hole central engine of the eight long GRBs.

4.1. Sub-GeV Loud

All but one (GRB 090102) of the eight long GRBs show significant emission in the LAT energy range of 30 MeV to several GeV (see the light curves in Figure 5 in the Appendix). We note that there is no redshift preference for these LAT-detected GRBs (see Figure 2; also refer to Ajello et al. 2019), which implies that long GRBs with such high-energy emissions are produced in different epochs of the universe. This affirms the positive correlation between the strong LAT emission and the high burst energetics, which may further imply that the central engines of such highly energetic bursts are most likely black holes.

4.2. X-Ray Afterglow Light Curves

The Neil Gehrels Swift Observatory/XRT can be slewed to the target within tens of seconds and hence provides observations of the early afterglow phase of GRBs in X-rays. The XRT observations have revealed features like flares, plateau, steep decay etc. in the flux light curves, which are related to the continued activity of the central engine well beyond the timescale of the prompt emission (Yamazaki et al. 2020). In several studies, these features are explained within the framework of both black hole (Kumar et al. 2008; Nathanail et al. 2016; Lei et al. 2017) and magnetar (Barniol Duran & Kumar 2009; Rowlinson et al. 2014; Li et al. 2018; Sarin et al. 2019; Zhao et al. 2020) central engine models. Generally, the observance of plateau and the steep decay thereafter have been interpreted as potential signatures of a magnetar where the plateau is produced by the energy injection from the magnetospheric wind, whereas the post-plateau steep decay signifies the collapse of the magnetar to a black hole (Rowlinson et al. 2014; Bernardini 2015; Chen et al. 2017).

Since the X-ray afterglow light curves are considered to shed some light on the central engine, we have extracted the XRT flux light curves[7] of these black holes candidates and shown them in Figure 3. The observational features in XRT light curves for the black hole cases are reported in Table 1. We note the following key points in these X-ray light curves: (i) neither shallow decay feature like plateau nor steep decays are observed; (ii) flares are observed in two cases as early as less than a few hundred seconds; (iii) apart from the jet break, multiple other breaks are observed in the flux light curves.

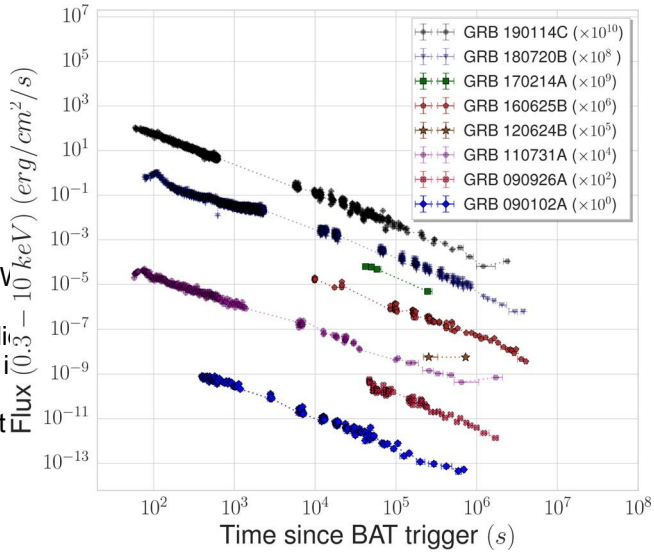

Figure 3. X-ray afterglow light curves of the eight long GRBs with black hole central engines, observed by the XRT instrument, are shown.

4.3. Properties of the Black Hole Central Engine

With the black hole as the central engine, the powering of the jet can happen via two main mechanisms: neutrino annihilation in a neutrino-dominated accretion flow (Ruffert et al. 1997; Chen & Beloborodov 2007), or by extracting the rotational energy of the Kerr black hole (Lee et al. 2000; Alexander et al. 2017). However, the first process has not been found to produce ultra-relativistic GRB jets (Leng & Giannios 2014) successfully. Therefore, we consider that the observed prompt emission is dominantly powered by the rotational energy, $E_{\rm rot}$, of the black hole central engine, such that

$$\eta E_{\rm rot} = E_{g,\rm beam} \qquad (5)$$

where η represents the net efficiency of converting the rotational energy of the black hole into the observed gamma-ray emission of the GRB and

$$E_{\rm rot} = f(a_*)\,\frac{M_*}{M_\odot}\,c^2 = 1.8' \ 10^{54}\, f_{\rm rot}(a_*)\,\frac{M_*}{M_\odot}\ {\rm erg} \qquad (6)$$

where M_* is the mass of the black hole and

$$f(a_*) = 1 - \sqrt{(1 + \sqrt{1 - a_*^2})/2} \qquad (7)$$

where $a_* = Jc/GM_*^2$ is the dimensionless black hole spin parameter, J is the angular momentum of the black hole.

4.3.1. Jet-powering Efficiency, η

The efficiency η is dominated by two main factors: (i) the fraction (κ) of the $E_{\rm rot}$ that is channeled into powering the relativistic jet, which depends on the mechanism of how the rotational energy is extracted, and (ii) the fraction of the jet power (ò) that is eventually radiated away in gamma-rays only. In the five cases where the kinetic energy estimates of the bursts that are evaluated using the multiwavelength data of the afterglow observations are available in the literature, we have used those values to estimate the respective radiation efficiency of the bursts. In three GRBs where the kinetic energy estimates of the bursts are not available in the literature, we adopted the average (ò = 0.65) of the ò values found for the other five GRBs (Table 1). We find this average value of ò to be consistent with the previous studies of the estimates of radiation efficiencies of hyper-energetic GRBs detected by Fermi (Racusin et al. 2011; Cenko et al. 2011). The hyper-accreting black holes formed during the GRB events are considered to be initially moderately spinning with $a_* = 0.5$, which later spins up close to maximal spin of $a_* = 0.9$ (Narayan et al. 1992; MacFadyen & Woosley 1999; Shapiro & Shibata 2002; Shibata & Shapiro 2002). In core collapse of massive stars, stellar-mass black holes are formed when the remnant core exceeds the maximum possible mass of a stable NS that can be formed. The maximum mass of an NS observed until date is 2.14 $M_\odot$ (Cromartie et al. 2020).

Inserting the above reasonable values for ò and κ for the minimum possible mass of the black hole, 2.14 $M_\odot$, in the

[7] XRT online repository, https://www.swift.ac.uk/xrt_curves/.

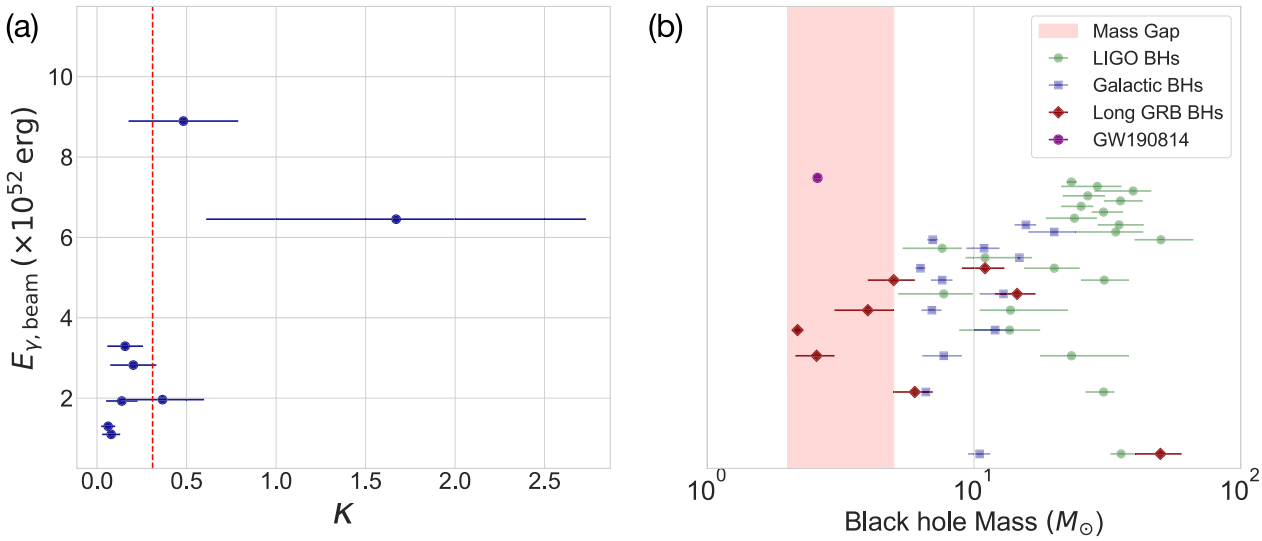

Figure 4. (a) GRB prompt emission energy, $E_{\gamma,\mathrm{beam}}$, vs. the jet-powering efficiency, κ is shown. The possible parameter space of κ is represented by the limits of the error bar, the mean of these limits are marked by the solid black circles. The maximum efficiency of the BZ mechanism is marked by the red dashed line. (b) The estimated parameter space of the mass of the black hole central engines of the eight long GRBs listed in the Table 1 are represented by the limits of the error bars mean of these limits are marked by the dark red diamonds. For comparison, masses of the black holes observed by LIGO in binary black hole mergers (Abbott et al. 2019), and the masses of the galactic black holes estimated in X-ray binaries (Wiktorowicz et al. 2014), are shown in green circles and blue squares, respect The secondary merger component of unknown nature detected by LIGO in GW190814 is shown in the purple circle (Abbott et al. 2020).

Equations (5) and (6) we estimate the parameter space of the jet-production efficiency, κ. The obtained results are shown in Figure 4(a). The high burst energetics require that a large amount of rotational energy is extracted from the black hole. This is reflected in the positive correlation obtained between κ and the burst energies of the GRBs. For some of the brightest GRBs with $E_{\gamma,\mathrm{beam}} \geq 2 \times 10^{52}$ erg, we find the upper limits of κ to range between 30% and 270%. The maximum fraction of the rotational energy of a black hole that can be extracted by a Blandford–Znajek (BZ) mechanism is 0.31 (Lee et al. 2000). Therefore, such high values of κ imply either of the two possibilities: (i) the masses of the black hole central engines are much larger than 2 $M_\odot$ (in other words, for smaller values of κ in these cases require that the rest mass energy of the black holes are much larger); or (ii) there are in addition other sources of energy powering the jet.

4.3.2. Black Hole Mass Estimate

The BZ process has been widely discussed in the literature as the potential mechanism to extract the rotational energy of a Kerr black hole (Blandford & Znajek 1977; Lee et al. 2000; McKinney 2005). In such a scenario, the jet-powering efficiency, κ, can be further understood as the product of two main factors: (i) The fraction of the rotational energy of the black hole that can be extracted by BZ process. Because these bursts are extremely energetic, it is reasonable to assume that the BZ mechanism works at its maximum efficiency; in other words, it can extract nearly 31% of the rotational energy of the black hole (Lee et al. 2000). (ii) The fraction of the extracted BZ power that gets channeled into the formation of the GRB jet. Numerical simulation studies show that for a black hole spin of $a = [0.5, 0.9]$, the efficiency of converting the extracted BZ power to a jet is found to be [7%–47%] (McKinney 2005).

Taking into account these different efficiency factors of κ and ò, we find η to range between 0.4% and 14% and we estimate the mass of the black hole central engine in these eight long GRBs using Equations (5) and (6). We find the masses of the black holes to range between 2 and 60 $M_\odot$. The values are listed in Table 1 and are also plotted in Figure 4(b).

The observational measurements of the masses of the compact remnants, post the core collapse of massive stars and the merger of compact objects like binary NS or NS—black hole, have shown a "gap" between the heaviest NSs and the lightest black holes. This is generally referred to as the "mass gap" region, which lies between 2 and 5 $M_\odot$ (Özel et al. 2012). The recent gravitational wave event, GW190814, detected by LIGO signifies the merger of two objects of masses 22.2–24.3 $M_\odot$ and 2.50–2.67 $M_\odot$ (Abbott et al. 2020). However, it is uncertain whether the lighter object is a massive NS or the lightest black hole. We find that the lighter black holes estimated in this study have possible masses close to the upper limit of the NS mass. Thus, we find that some of the black holes formed in these catastrophic events of GRBs can be the likely candidates to lie in the mass gap region.

5. Summary

Despite several decades of extensive studies and observations of gamma-ray bursts, many aspects of the event still remain largely a mystery. One of these is regarding the central engine powering the ultra-relativistic GRB jets whose luminosities exceed the Eddington luminosity by several orders of magnitude. Broadly, the possible central engine is classified into either a magnetar or a black hole. Much work has been done to investigate these possibilities by studying various features such as plateau and its post steep decay, flares present in the X-ray afterglow light curves, etc. However, these studies have remained mostly inconclusive and ambiguous with both magnetar and black hole models being able to explain the observed features.

One robust way to identify GRBs with a black hole central engine is by looking at the energetics of the GRB event. The maximum possible rotational energy of the magnetar that can be converted into a relativistic jet is $\sim 10^{52}$ erg. In this work, we use this constraint to identify the GRBs whose beam-corrected

prompt emission energetics exceed this energy budget. Eight long GRBs are found to possess burst energies greater than 10^{52} erg and thereby central engines that are most likely black holes. We note that these GRBs are extremely bright with significant emission in the sub-GeV energy range. The X-ray afterglow light curves of these GRBs do not show any "plateau" and steep decay-like features. Popularly, such features are associated with the activity of a magnetar central engine. So, the non-observance of these features further asserts that the central engines of these GRBs are black holes. Considering that the jet is dominantly powered by the rotational energy of the black hole, which is extracted by the BZ mechanism, we estimate the masses of the black holes to range between 2 and 60 $M_\odot$. We find that the lighter black holes formed in these catastrophic events could be candidates to lie in the mass gap between the heaviest known NS and the lightest known black hole.

We would like to thank Prof. Pawan Kumar and Dr. Vikas Chand for the suggestions. This research has made use of Fermi data obtained through High Energy Astrophysics Science Archive Research Center Online Service, provided by the NASA/Goddard Space Flight Center. This publication uses data from the Neil Gehrels Swift Observatory mission, archived at the Swift Data Center (SDC) at the Goddard Space Flight Center (GSFC). This work utilized various software such as HEASARC, XSPEC, Python, astropy, corner, numpy, scipy, matplotlib, FTOOLS etc. Light curve and spectral analysis are performed using multi-mission maximum likelihood framework (3ML; Vianello et al. 2015).

Appendix A
Light Curves

The prompt emission light curves of the eight GRBs as detected by Fermi GBM and LAT are presented in Figure 5.

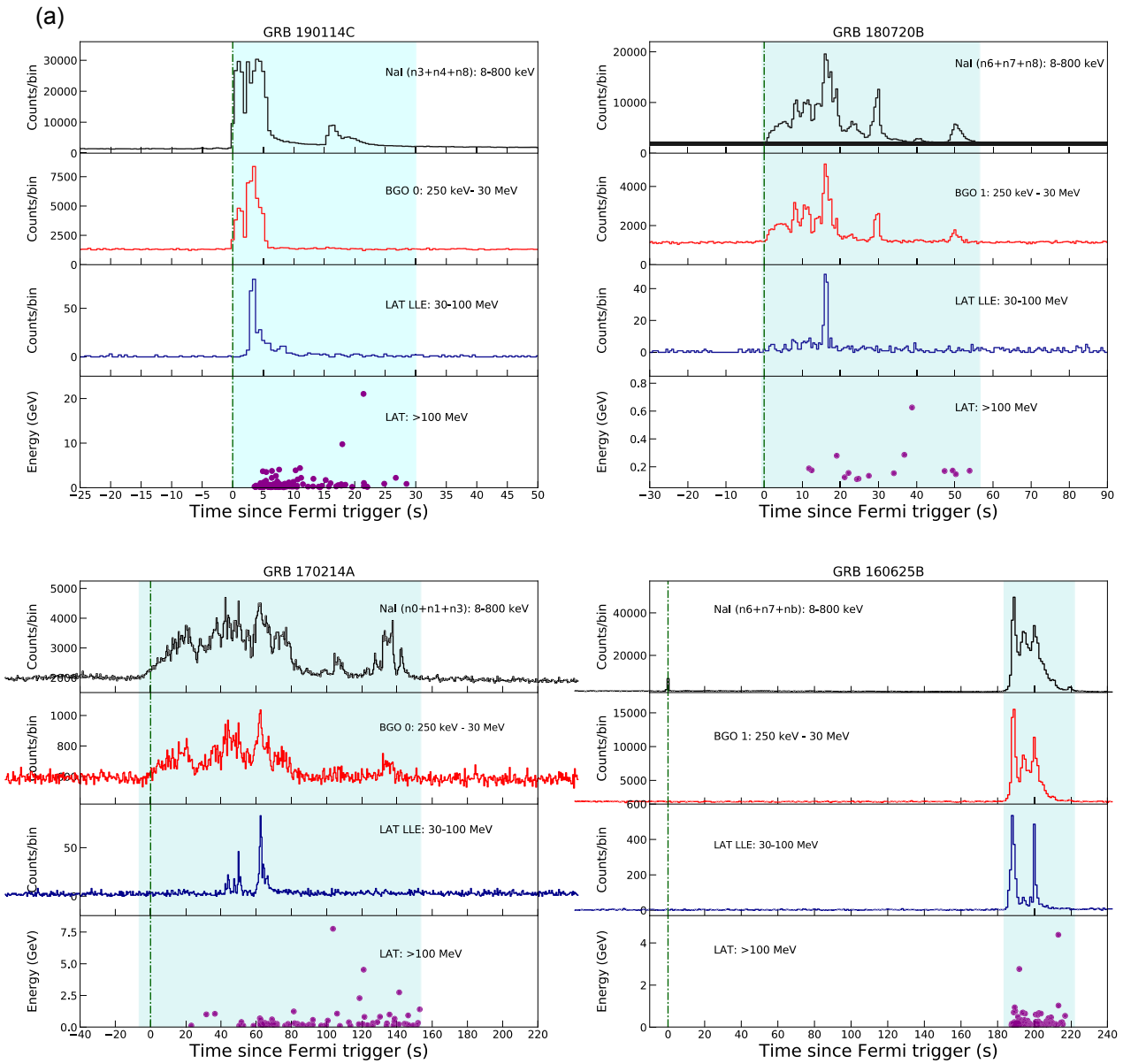

Figure 5. Light curves of the eight GRBs with the black hole as a central engine: NaI, BGO, and LLE light curves are presented in black, red, and blue color, respectively, from top to bottom. In the bottom panel of each GRB light curve, LAT photons are shown in magenta color with energy (in GeV) information on the y-axis. The cyan shaded region marks the time interval used for time-integrated spectral analysis, and the green vertical line represents the trigger time of the GRB.

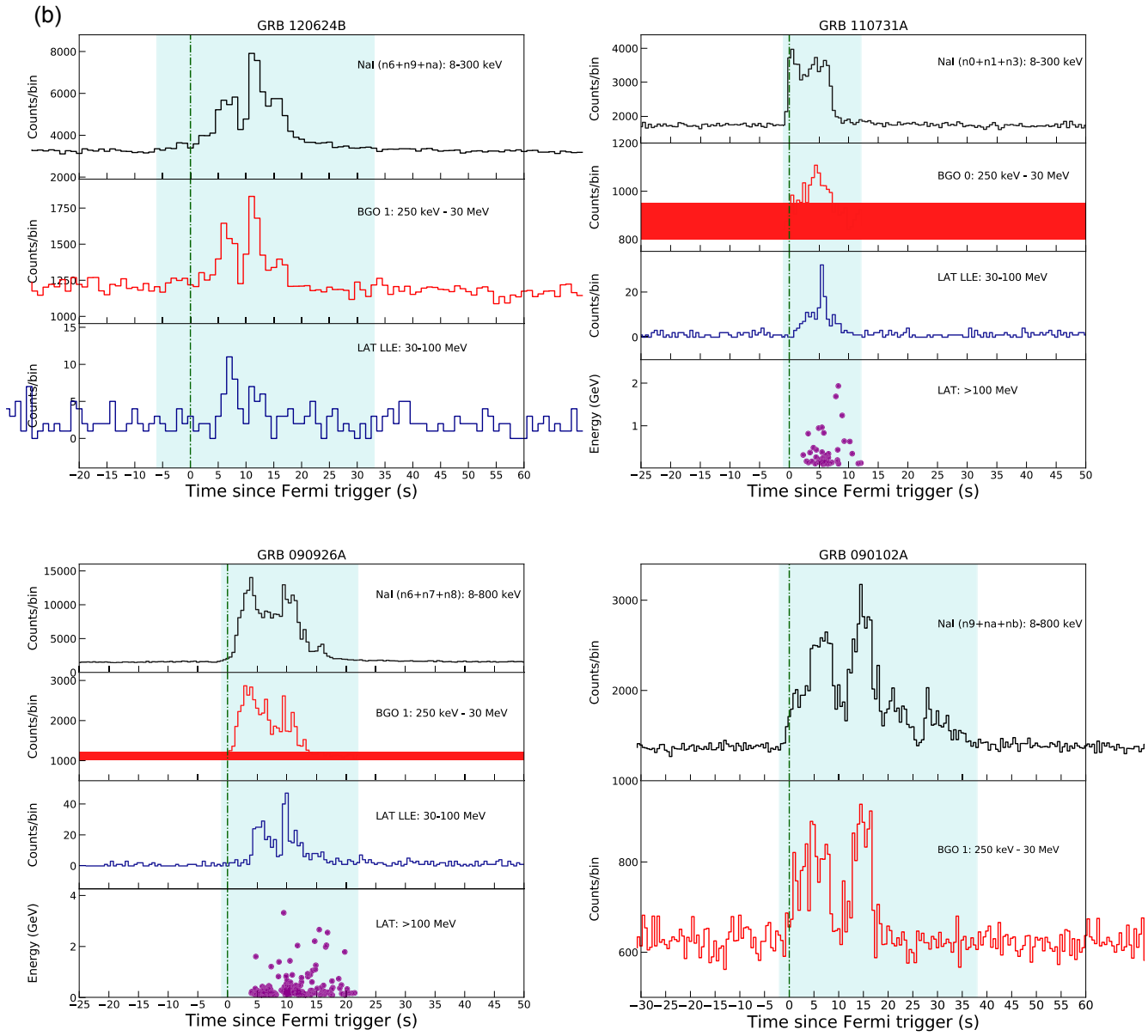

Figure 5. (Continued.)

Appendix B
Potential Limitations and Caveats

Below we discuss the different caveats that are involved in the estimation of the beam-corrected total energy of the bursts, $E_{\gamma,\mathrm{beam}}$.

1. Bolometric fluence. In general, the burst fluence of Fermi-detected GRBs are reported in the energy range 10–1000 keV, which is a small energy window. Therefore, in order to assess the total energy of the GRB, we estimate the bolometric fluence by extrapolating the spectrum determined in the Fermi energy window (GBM: 8 keV–40 MeV) to an energy interval of 1 keV–1 GeV. In case of GRBs with LAT detections with the highest energy photons greater than 1 GeV, the bolometric fluence is estimated for the energy interval until that highest energy value. We note that among the final eight LAT-detected long GRBs excepting GRB 120624B (until LAT low-energy events (LLE), 100 MeV) and GRB 090102A (GBM only), the spectrum is well constrained until 1 GeV and therefore, their bolometric fluence estimates are robust. For the 135 GRBs with known redshifts in our study, the median of the ratio of bolometric fluence to the Fermi catalog fluence in the energy range, 10–1000 keV, is found to be nearly 3. The ratio of the fluences is found to range between 1 and 45, as shown in Figure 6.
2. Jet-opening angle and viewing geometry. It has been shown by the van Eerten et al. (2010) and Ryan et al. (2015) studies that it is likely to view the jet off-axis at a significant fraction of the jet-opening angle. This can smear out the possible jetbreak and produce a smooth transition into the post jet-break flux decay, which is likely to be visible in a time span beyond the typical viewing window of Neil Gehrels Swift Observatory XRT (10 days). This may lead to overestimation of the jet-

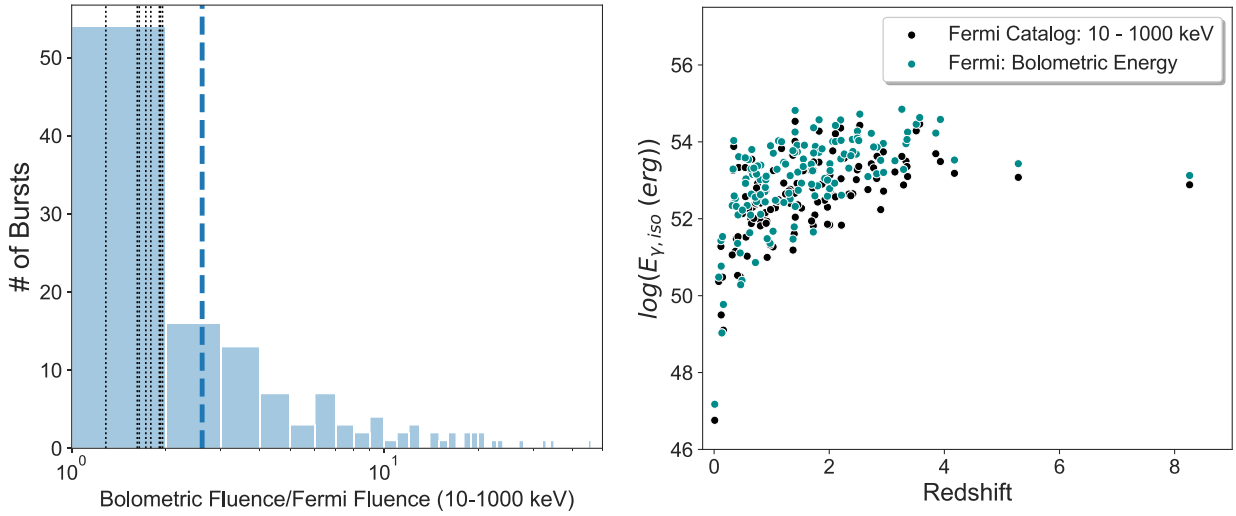

Figure 6. (a) The distribution of the ratio of bolometric fluence to the Fermi catalog fluence is shown in the left panel. The median value of the distribution is ~3 and presented with blue dashed vertical line. The fluence ratio for the final eight GRBs listed in the Table 1 ranging between 1.3 and 2 are shown in black dotted vertica lines. (b) The isotropic burst energies estimated using the fluence in the energy range 10–1000 keV and bolometric fluence in the energy range 1 keV–1 GeV or observed energy range (LLE GRBs observed above 1 GeV) are shown in black and teal circles, respectively, with respect to the measured redshift.

opening angle and thereby affect the estimated beam-corrected energy of the GRB. This caveat is more relevant in cases where a clear achromatic jet break is not observed, and where we have estimated a lower limit on the je-opening angle assuming on-axis viewing geometry.

3. Structured jet. The collimated GRB outflow can be in the form of either a uniform (top-hat) or a structured jet (Granot et al. 2002). In case of a uniform jet, the total energy of the outflow is confined to a certain solid angle corresponding to an opening angle of θ_j. On the other hand, in case of a structured jet, the jet energy or Lorentz factor remains a constant within the jet-core, θ_c and beyond that there exists a certain structure such as a decaying Lorentz factor or jet energy with respect to the angle measured from the jet axis (Figure 7) until θ_j. The GRB will be visible only when the line of sight of the observer is within the $\theta_j + 1/\Gamma(\theta_j)$.

In the case of a structured jet, for an off-axis observer when the viewing angle, $\theta_c < \theta_v < \theta_j$, the observed prompt energy flux of the burst is lower relative to the scenario when $\theta_v < \theta_c$. Thus, the $E_{\gamma,iso}$ estimate done in such a case will be a lower limit of the actual total burst energy. For an on-axis observer, when these bursts have their jet core pointed toward the observer (i.e. $\theta_v < \theta_c$). The prominent jet break observed in the late-time afterglow emission can be then related to the scenario when $1/\Gamma(\theta_v - \theta_c) = \theta_j$ (Peng et al. 2005). Because in a structured jet, the energy injection (E) and Γ is angle dependent within the θ_j, the $E_{\gamma,iso}$ estimate as well as the beaming correction applied on the $E_{\gamma,iso}$ would give an overestimation of the true burst energy ($E_{\gamma,beam}$). However, to get a correct estimate of the burst energy, one should know the profile of the jet and the viewing angle. These estimates are generally difficult because of the degeneracy between various model parameters and currently out of the scope of this work.

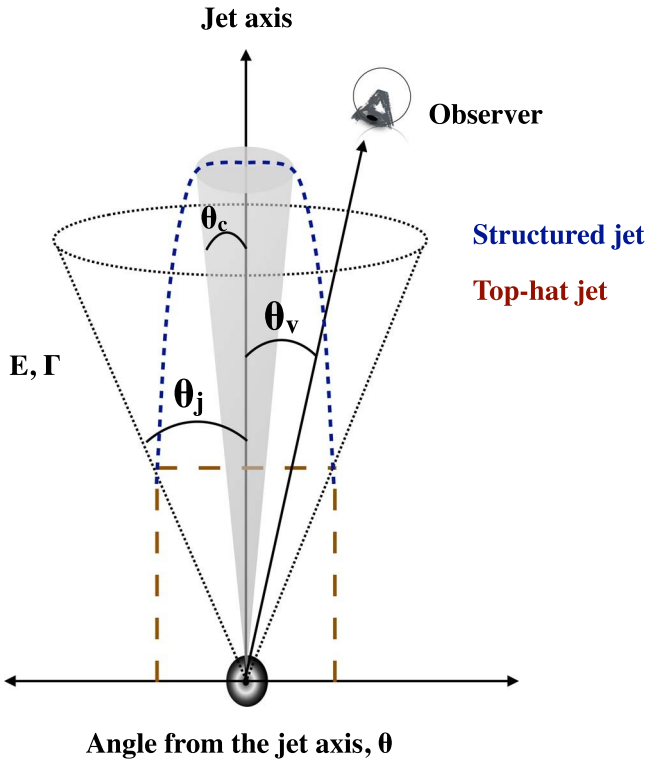

Figure 7. Illustration of a collimated GRB outflow with an opening angle, θ_j, is shown. In the case of a top-hat jet model, both the jet energy, E, and Lorentz factor, Γ, are angle independent (i.e., constant, shown in brown long dashed line) within the θ_j. On the other hand, in case of a structured jet model, the E or Γ remains a constant within the jet core, θ_c and beyond that possess a certain profile until θ_j (shown by the blue short dashed line), θ_v is the viewing angle as measured from the jet axis.

Appendix C

The details of the 135 GRBs with known redshift and detected by Fermi during the years 2008-2019 are listed in the Table 2.

Table 2
Properties of 135 GRBs

S.No.	GRB Name	T_{90} (Fermi) (s)	z	LLE/LAT	Fluence (erg cm^{-2})	$E_{\gamma,iso}$ log(E in erg)	θ_j °	Reference	$E_{\gamma,beam}$ log(E in erg)
1	191011A	25.09	1.722	NO	5.87E−07	51.66	L	L	L
2	190829A	59.39	0.0785	NO	2.01E−05	50.48	L	L	L
3	190719C	175.62	2.469	NO	3.29E−05	53.68	$3.2^{+0.5}_{0.5}$	This work	50.88
4	190114C	116.35	0.425	YES	8.45E−04	53.62	>32.5	Misra et al. (2019)	52.81
5	181020A	15.10	2.938	NO	4.66E−05	53.96	$1.4^{+0.2}_{0.2}$	This work	50.46
6	181010A	9.73	1.39	NO	1.18E−06	51.79	L	L	L
7	180728A	6.4	0.117	NO	7.91E−05	51.43	L	L	L
8	180720B	48.9	0.654	YES	5.34E−04	53.80	>17.2	This work	52.44
9	180703A	20.74	0.6678	NO	1.15E−04	53.15	>7.5	This work	51.09
10	180620B	46.72	1.1175	NO	3.10E−04	54.03	$5.9^{+0.0}_{0.9}$	This work	51.76
11	180314A	22.02	1.445	NO	9.87E−05	53.74	>9.2	This work	51.86
12	180205A	15.36	1.409	NO	3.91E−06	52.32	L	L	L
13	171222A	80.38	2.409	NO	4.01E−05	53.75	>8.2	This work	51.75
14	171010A	107.27	0.3285	YES	6.85E−04	53.29	>6	Chand et al.(2019)	51.16
15	170903A	25.6	0.886	NO	1.26E−05	52.44	L	L	L
16	170817A	2.05	0.0093	NO	7.3E−07	47.18	L	L	L
17	170705A	22.78	2.01	NO	2.64E−05	53.43	>12.4	This work	51.80
18	170607A	20.93	0.632	NO	1.13E−05	52.10	L	L	L
19	170405A	78.59	3.51	YES	1.10E−04	54.46	$0.8^{+0.2}_{0.2}$	This work	50.45
20	170214A	122.88	2.53	YES	3.45E−04	54.72	>3.7	This work	52.04
21	170113A	49.15	1.968	NO	3.93E−06	52.59	$12^{+1.9}_{1.9}$	Li et al. (2018)	50.92
22	161129A	36.1	0.645	NO	3.82E−05	52.64	$2.3^{+0.3}_{0.3}$	This work	49.54
23	161117A	122.18	1.549	NO	5.61E−05	53.55	$4.7^{+0.1}_{0.1}$	Li et al. (2018)	51.08
24	161017A	37.89	2.013	NO	1.75E−05	53.25	$2.8^{+0.5}_{0.5}$	Tachibana et al(2018)	50.34
25	161014A	36.61	2.823	NO	8.1E−06	53.17	$2.2^{+0.3}_{0.3}$	This work	50.04
26	160821B	1.088	0.16	NO	9.11E−07	49.77	L	L	L
27	160804A	131.59	0.736	NO	1.86E−05	52.45	L	L	L
28	160629A	64.77	3.332	NO	3.73E−05	53.95	>2.9	This work	51.06
29	160625B	453.38	1.406	YES	1.24E−03	54.82	$3.6^{+0.2}_{0.2}$	Alexander et al.(2017)	52.11
30	160624A	0.38	0.483	NO	3.92E−07	50.40	L	L	L
31	160623A	107.78	0.367	YES	9.24E−05	52.53	$13^{+2.8}_{2.8}$	Chen et al.(2020)	50.93
32	160509A	369.67	1.17	YES	2.69E−04	54.00	$3.9^{+0.2}_{0.2}$	Laskar et al.(2016)	51.37
33	151027A	123.39	0.81	NO	1.36E−04	53.39	$7.7^{+0.2}_{0.2}$	Li et al. (2018)	51.35
34	150821A	103.43	0.755	NO	1.5E−04	53.37	$0.7^{+0.2}_{0.2}$	This work	49.27
35	150727A	49.41	0.313	NO	8.49E−05	52.34	L	L	L
36	150514A	10.81	0.807	YES	7.22E−06	52.17	L	L	L
37	150403A	22.27	2.06	YES	9.57E−05	54.01	7.74	Pisani et al.(2016)	51.97
38	150314A	10.69	1.758	YES	9.48E−05	53.88	$0.7^{+0.1}_{0.1}$	This work	49.79
39	150301B	13.31	1.5169	NO	1.38E−05	52.93	>4.3	This work	50.38
40	150120A	3.33	0.46	NO	3.35E−07	50.28	L	L	L
41	150101B	0.08	0.134	NO	2.38E−07	49.03	L	L	L
42	141225A	56.32	0.915	NO	5.78E−05	53.13	>4.9	This work	50.69
43	141221A	23.81	1.452	NO	2.9E−05	53.21	>5.8	This work	50.92
44	141220A	7.67	1.3195	NO	6.93E−06	52.51	>6.6	This work	50.34
45	141028A	31.49	1.82	YES	6.26E−05	53.73	>7.5	This work	51.66
46	141004A	2.56	0.573	NO	2.46E−05	52.35	L	L	L
47	140907A	35.84	1.21	NO	6.64E−06	52.42	L	L	L
48	140808A	4.48	3.29	NO	8.17E−06	53.28.	>5.1	This work	50.89
49	140801A	7.17	1.32	NO	2.8E−05	53.12	>7.3	This work	51.03
50	140703A	83.97	3.14	NO	1.48E−05	53.51	$8.9^{+0.1}_{0.1}$	Li et al. (2018)	51.59
51	140623A	111.10	1.92	NO	1.2E−05	53.05	>9.1	This work	51.16
52	140620A	45.82	0.88	NO	2.36E−05	52.70	>11.7	This work	51.02
53	140606B	22.78	0.384	NO	5.3E−05	52.32	L	L	L
54	140512A	147.97	0.725	NO	1.0E−04	53.17	$6^{+0.1}_{0.1}$	Li et al. (2018)	50.90
55	140508A	44.29	1.027	NO	1.7E−04	53.71	>9.9	This work	51.88
56	140506A	64.13	0.889	NO	2.98E−05	52.82	>18.8	This work	51.54
57	140423A	95.23	3.26	NO	3.04E−04	54.85	>4.1	This work	52.25
58	140304A	31.23	5.283	NO	5.51E−06	53.43	$1.2^{+0.3}_{0.3}$	This work	49.74
59	140213A	18.62	1.2076	NO	7.4E−05	53.47	$4.6^{+1.3}_{1.3}$	This work	50.99
60	140206A	27.26	2.73	NO	9.65E−05	54.22	$2.9^{+0.5}_{0.5}$	This work	51.33
61	131231A	31.23	0.642	YES	1.75E−04	53.30	>8.7	This work	51.36

Table 2
(Continued)

S.No.	GRB Name	T_{90} (Fermi) (s)	z	LLE/LAT	Fluence (erg cm^{-2})	$E_{\gamma,iso}$ log(E in erg)	θ_j °	Reference	$E_{\gamma,beam}$ log(E in erg)
62	131108A	18.18	2.4	YES	8.33E−05	54.06	>5.2	This work	51.68
63	131105A	112.64	1.686	NO	3.55E−05	53.42	$4.3^{+0.1}_{0.1}$	Li et al. (2018)	50.86
64	131011A	77.06	1.874	NO	7.31E−05	53.82	>3.5	This work	51.09
65	131004A	1.15	0.717	NO	5.10E−07	50.86	L	L	L
66	130925A	215.56	0.347	NO	1.22E−04	52.59	>33	This work	52.01
67	130702A	58.88	0.145	YES	1.28E−04	51.54	L	L	L
68	130612A	7.42	2.006	NO	5.98E−06	52.78	$11.4^{+0.4}_{0.4}$	Li et al. (2018)	51.08
69	130610A	21.76	2.092	NO	7.72E−06	52.93	>6.9	This work	50.79
70	130518A	48.58	2.488	YES	1.28E−04	54.28	>4.9	This work	51.84
71	130427A	138.24	0.3399	YES	3.51E−03	54.03	>5	Perley et al.(2014)	< 52
72	130420A	104.96	1.297	NO	1.01E−05	52.66	$15.1^{+5.1}_{5.1}$	Li et al. (2018)	51.23
73	130215A	143.75	0.597	NO	3.52E−04	53.54	L	No XRT	L
74	121211A	5.63	1.023	NO	1.64E−06	51.68	L	L	L
75	121128A	17.34	2.2	NO	3.02E−05	53.56	$10.5^{+0.3}_{0.3}$	Li et al. (2018)	51.78
76	120909A	112.07	3.93	NO	1.23E−04	54.58	>3.2	This work	51.79
77	120907A	5.76	0.97	NO	8.91E−07	51.36	L	L	L
78	120811C	14.34	2.671	NO	7.5E−06	53.10	$6.4^{+0.02}_{0.02}$	Li et al. (2018)	50.89
79	120729A	25.47	0.8	YES	5.86E−05	53.02	$1.2^{+0.3}_{0.3}$	Wang et al.(2018)	49.34
80	120716A	226.05	2.486	NO	8.47E−05	54.10	>4.2	This work	51.53
81	120712A	22.53	4.1745	NO	9.83E−06	53.53	$5^{+0.02}_{0.02}$	Li et al. (2018)	51.10
82	120711A	44.03	1.405	YES	3.39E−04	54.26	>4.6	This work	51.77
83	120624B	271.36	2.1974	YES	3.11E−04	54.57	>5.9	This work	52.28
84	120326A	11.78	1.798	NO	8.57E−06	52.86	$4.6^{+0.2}_{0.2}$	Song et al.(2016)	50.36
85	120119A	55.3	1.728	NO	6.59E−05	53.71	$1.8^{+01}_{0.1}$	Song et al.(2018)	50.42
86	120118B	37.82	2.943	NO	8.18E−06	53.20	>8	This work	51.20
87	111228A	99.84	0.714	NO	2.58E−05	52.56	$7.3^{+0.2}_{0.2}$	Li et al. (2018)	50.47
88	111117A	0.43	2.211	NO	3.39E−06	52.61	6	Song et al.(2018)	50.35
89	111107A	12.03	2.893	NO	1.74E−05	53.52	>5.4	This work	51.17
90	110818A	67.07	3.36	NO	7.36E−05	54.25	$1.8^{+0.3}_{0.3}$	This work	50.93
91	110731A	7.48	2.83	YES	3.95E−05	53.86	$28.9^{+0.0}_{0.7}$	Zhang et al.(2015)	52.96
92	110213A	34.31	1.46	NO	9.65E−06	52.74	8.1	sSong et al2018	50.75
93	110128A	7.94	2.339	NO	1.56E−05	53.32	>8.9	This work	51.34
94	110106B	35.52	0.618	NO	4.11E−06	51.64	L	L	L
95	101219B	51.01	0.5519	NO	1.30E−04	53.04	17.1	Song & Liu (2019)	51.68
96	101213A	45.06	0.414	NO	2.73E−05	52.10	L	L	L
97	100906A	110.59	1.727	NO	2.99E−04	54.37	$4.4^{+0.1}_{0.1}$	Li et al. (2018)	51.84
98	100816A	2.04	0.8035	NO	2.37E−05	52.63	$28.2^{+0.02}_{3.7}$	Zhang et al.(2015)	51.71
99	100814A	150.53	1.44	NO	1.47E−04	53.91	$5.2^{+0.1}_{0.1}$	Li et al. (2018)	51.53
100	100728B	10.24	2.106	NO	9.18E−05	54.01	3.6	Song et al.(2018)	51.30
101	100728A	165.38	1.567	YES	1.26E−04	53.91	$1.6^{+0.3}_{0.3}$	This work	50.51
102	100625A	0.24	0.452	NO	2.33E−06	51.11	L	L	L
103	100615A	37.38	1.398	NO	8.7234E−06	52.66	$25.6^{+2.2}_{2.2}$	Zhang et al.(2015)	51.65
104	100414A	26.5	1.368	YES	1.17E−04	53.77	>8.2	This work	51.78
105	100206A	0.18	0.4068	NO	5.12E−06	51.36	L	L	L
106	100117A	0.26	0.92	NO	1.29E−06	51.48	L	L	L
107	091208B	12.48	1.063	YES	9.70E−06	52.48	7.3	Nemmen et al.(2012)	50.39
108	091127	8.7	0.49	NO	2.57E−05	52.23	L	L	L
109	091024	93.95	1.092	NO	5.91E−05	53.29	4.07	Song et al.(2018)	50.69
110	091020	24.26	1.71	NO	2.31E−05	53.25	6.9	Nemmen et al.(2012)	51.11
111	091003A	20.22	0.8969	YES	4.63E−05	53.01	>14.1	This work	51.50
112	090927	0.51	1.37	NO	5.84E−07	51.47	L	L	L
113	090926B	64.0	1.24	NO	6.31E−05	53.42	$0.4^{+0.1}_{0.1}$	This work	48.73
114	090926	13.76	2.1062	YES	2.41E−04	54.43	9^{+4}_{2}	Cenko et al.(2011)	52.52
115	090902B	19.33	1.822	YES	4.37E−04	54.57	$3.9^{+0.2}_{0.2}$	Cenko et al.(2011)	51.94
116	090618	112.39	0.54	NO	4.81E−04	53.59	6.7	Nemmen et al.(2012)	51.42
117	090516	123.14	3.85	NO	5.59E−05	54.23	$3.5^{+0.1}_{0.1}$	Li et al. (2018)	51.50
118	090510	0.96	0.903	YES	5.64E−05	53.11	$14.1^{+0.1}_{0.1}$	Li et al. (2018)	51.58
119	090424	14.14	0.544	NO	1.03E−04	52.92	6.7	Nemmen et al.(2012)	50.76
120	090423	7.17	8.26	NO	1.43E−06	53.13	$22.5^{+0.6}_{15.1}$	Zhang et al.(2015)	52.01
121	090328	61.7	0.736	YES	9.66E−05	53.16	$4.2^{+1.3}_{0.8}$	Cenko et al.(2011)	50.59

Table 2
(Continued)

S.No.	GRB Name	T_{90} (Fermi) (s)	z	LLE/LAT	Fluence (erg cm^{-2})	$E_{\gamma,iso}$ log(E in erg)	θ_j °	Reference	$E_{\gamma,beam}$ log(E in erg)
122	090323	133.89	3.57	YES	1.60E−04	54.63	$2.8^{+0.4}_{0.1}$	Cenko et al.(2011)	51.71
123	090113	17.41	1.7493	NO	4.95E−06	52.60	$6.9^{+7.8}_{4.1}$	Zhang et al.(2015)	50.46
124	090102	26.62	1.547	YES	3.59E−05	53.36	$23.9^{+1.1}_{12.1}$	Zhang et al.(2015)	52.29
125	081222	18.88	2.77	NO	4.17E−05	53.87	2.8	Nemmen et al.(2012)	50.94
126	081221	29.7	2.26	NO	3.86E−05	53.68	$4.3^{+0.1}_{0.1}$	Li et al. (2018)	51.12
127	081121	41.98	2.512	NO	7.19E−05	54.03	>7.4	This work	51.95
128	081109	58.37	0.9787	NO	2.99E−04	53.90	>7.5	This work	51.83
129	081008	126.72	1.9685	NO	5.88E−05	53.01	$6.1^{+0.3}_{0.3}$	Li et al. (2018)	50.76
130	080928	14.34	1.692	NO	1.06E−05	52.90	$2.4^{+0.4}_{0.4}$	This work	49.82
131	080916A	46.34	0.689	NO	1.58E−04	53.32	>14.9	This work	51.84
132	080905B	105.98	2.374	NO	3.2E−05	53.64	L	L	L
133	080905A	0.96	0.1218	NO	1.58E−05	50.77	$6.7^{+0.2}_{0.2}$	Li et al. (2018)	51.48
134	080810	75.20	3.35	NO	4.76E−05	54.06	3.83	Song et al.(2018)	51.41
135	080804	24.70	2.2045	NO	9.11E−05	54.04	$2.9^{+0.8}_{0.8}$	Wang et al.(2018)	51.16

ORCID iDs

Vidushi Sharma https://orcid.org/0000-0002-4394-4138
Shabnam Iyyani https://orcid.org/0000-0002-2525-3464
Dipankar Bhattacharya https://orcid.org/0000-0003-3352-3142

References

Abbott, B. P., Abbott, R., Abbott, T. D., et al. 2019, ApJL, 882, L24
Abbott, R., Abbott, T., Abraham, S., et al. 2020, ApJL, 896, L44
Aghanim, N., Akrami, Y., Ashdown, M., et al. 2020, A&A, 641, A6
Ajello, M., Arimoto, M., Axelsson, M., et al. 2019, ApJ, 878, 52
Alexander, K. D., Laskar, T., Berger, E., et al. 2017, ApJ, 848, 69
Barniol Duran, R., & Kumar, P. 2009, MNRAS, 395, 955
Beniamini, P., Giannios, D., & Metzger, B. D. 2017, MNRAS, 472, 3058
Bernardini, M. G. 2015, JHEAp, 7, 64
Blandford, R. D., & Znajek, R. L. 1977, MNRAS, 179, 433
Bloom, J. S., Frail, D. A., & Sari, R. 2001, AJ, 121, 2879
Cenko, S., Frail, D., Harrison, F., et al. 2011, ApJ, 732, 29
Chakrabarty, D. 2008, in AIP Conf. Ser. 1068, A Decade of Accreting Millisecond X-Ray Pulsars, ed. R. Wijnands et al. (Melville, NY: AIP), 67
Chand, V., Chattopadhyay, T., Oganesyan, G., et al. 2019, ApJ, 874, 70
Chen, W., Xie, W., Lei, W.-H., et al. 2017, ApJ, 849, 119
Chen, W. J., Urata, Y., Huang, K., et al. 2020, ApJL, 891, L15
Chen, W.-X., & Beloborodov, A. M. 2007, ApJ, 657, 383
Cromartie, H. T., Fonseca, E., Ransom, S. M., et al. 2020, NatAs, 4, 72
Cunningham, V., Cenko, S. B., Ryan, G., et al. 2020, ApJ, 904, 166
Duncan, R. C., & Thompson, C. 1992, ApJL, 392, L9
Evans, P., Beardmore, A., Page, K., et al. 2009, MNRAS, 397, 1177
Evans, P., Beardmore, A., Page, K. L., et al. 2007, A&A, 469, 379
Frail, D. A., Kulkarni, S., Sari, R., et al. 2001, ApJL, 562, L55
Goldstein, A., Connaughton, V., Briggs, M. S., & Burns, E. 2016, ApJ, 818, 18
Granot, J., Panaitescu, A., Kumar, P., & Woosley, S. E. 2002, ApJL, 570, L61
Hessels, J. W. T., Ransom, S. M., Stairs, I. H., et al. 2006, Sci, 311, 1901
Kumar, P., Narayan, R., & Johnson, J. L. 2008, MNRAS, 388, 1729
Laskar, T., Alexander, K. D., Berger, E., et al. 2016, ApJ, 833, 88
Lee, H. K., Wijers, R. A. M. J., & Brown, G. E. 2000, PhR, 325, 83
Lei, W.-H., Zhang, B., Wu, X.-F., & Liang, E.-W. 2017, ApJ, 849, 47
Leng, M., & Giannios, D. 2014, MNRAS, 445, L1
Li, L., Wu, X.-F., Lei, W.-H., et al. 2018, ApJS, 236, 26
MacFadyen, A. I., & Woosley, S. E. 1999, ApJ, 524, 262
MacLachlan, G. A., Shenoy, A., Sonbas, E., et al. 2013, MNRAS, 432, 857
McKinney, J. C. 2005, arXiv:astro-ph/0506369
Meszaros, P. 2006, RPPh, 69, 2259
Metzger, B., Giannios, D., Thompson, T., Bucciantini, N., & Quataert, E. 2011, MNRAS, 413, 2031
Metzger, B. D. 2017, LRR, 20, 3
Metzger, B. D., Beniamini, P., & Giannios, D. 2018, ApJ, 857, 95
Misra, K., Resmi, L., Kann, D., et al. 2019, arXiv:1911.09719
Narayan, R., Paczynski, B., & Piran, T. 1992, ApJL, 395, L83
Narayan, R., Piran, T., & Kumar, P. 2001, ApJ, 557, 949
Nathanail, A., Strantzalis, A., & Contopoulos, I. 2016, MNRAS, 455, 4479
Nemmen, R. S., Georganopoulos, M., Guiriec, S., et al. 2012, Sci, 338, 1445
Özel, F., Psaltis, D., Narayan, R., & Santos Villarreal, A. 2012, ApJ, 757, 55
Papitto, A., Torres, D. F., Rea, N., & Tauris, T. M. 2014, A&A, 566, A64
Patruno, A., Haskell, B., & Andersson, N. 2017, ApJ, 850, 106
Peng, F., Königl, A., & Granot, J. 2005, ApJ, 626, 966
Perley, D. A., Cenko, S. B., Corsi, A., et al. 2014, ApJ, 781, 37
Pisani, G., Ruffini, R., Aimuratov, Y., et al. 2016, ApJ, 833, 159
Racusin, J. L., Oates, S. R., Schady, P., et al. 2011, ApJ, 738, 138
Rowlinson, A., Gompertz, B. P., Dainotti, M., et al. 2014, MNRAS, 443, 1779
Ruffert, M., Janka, H. T., Takahashi, K., & Schaefer, G. 1997, A&A, 319, 122
Ryan, G., van Eerten, H., MacFadyen, A., & Zhang, B.-B. 2015, ApJ, 799, 3
Sari, R., Piran, T., & Halpern, J. 1999, ApJL, 519, L17
Sarin, N., Lasky, P. D., & Ashton, G. 2019, ApJ, 872, 114
Shapiro, S. L., & Shibata, M. 2002, ApJ, 577, 904
Shibata, M., & Shapiro, S. L. 2002, ApJL, 572, L39
Song, C.-Y., & Liu, T. 2019, ApJ, 871, 117
Song, C.-Y., Liu, T., Gu, W.-M., & Tian, J.-X. 2016, MNRAS, 458, 1921
Song, C.-Y., Liu, T., & Li, A. 2018, MNRAS, 477, 2173
Tachibana, Y., Arimoto, M., Asano, K., et al. 2018, PASJ, 70, 92
Usov, V. V. 1992, Natur, 357, 472
van Eerten, H., Zhang, W., & MacFadyen, A. 2010, ApJ, 722, 235
Vianello, G., Lauer, R. J., & Younk, P. 2015, arXiv:1507.08343
Wang, X.-G., Zhang, B., Liang, E.-W., et al. 2015, ApJS, 219, 9
Wang, X.-G., Zhang, B., Liang, E.-W., et al. 2018, ApJ, 859, 160
Wiktorowicz, G., Belczynski, K., & Maccarone, T. 2014, in Binary Systems, their Evolution and Environments (Beijing: Chinese Academy Of Sciences), 37
Woosley, S. 1993, ApJ, 405, 273
Yamazaki, R., Sato, Y., Sakamoto, T., & Serino, M. 2020, MNRAS, 494, 5259
Zhang, B.-B., Van Eerten, H., Burrows, D. N., et al. 2015, ApJ, 806, 15
Zhao, L., Liu, L., Gao, H., et al. 2020, ApJ, 896, 42